Synthesis of TiB_2-Ni_3B nanocomposite coating by DC magnetron sputtering for corrosion-erosion protection

To cite this article: Jorge Morales Hernández *et al* 2021 *Mater. Res. Express* **8** 126403

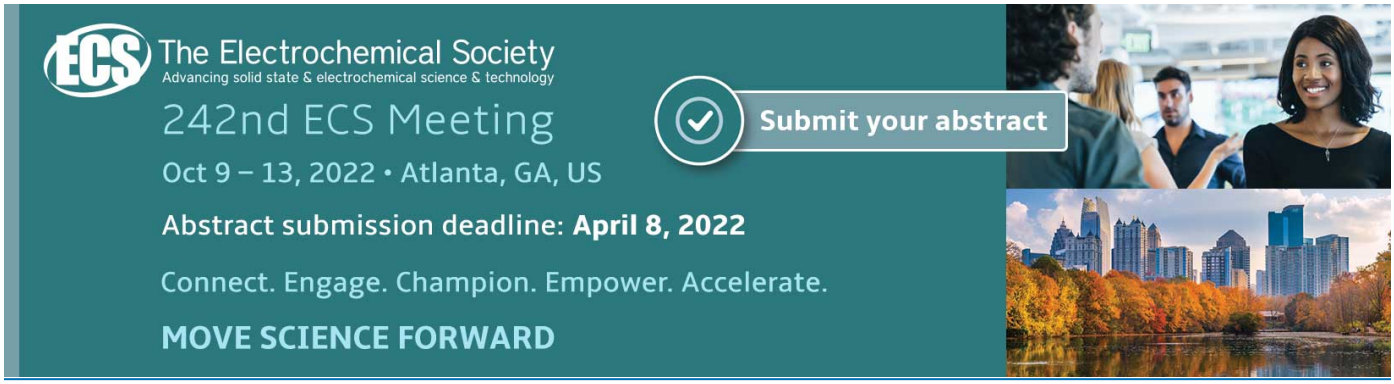

Materials Research Express

PAPER

Synthesis of TiB_2-Ni_3B nanocomposite coating by DC magnetron sputtering for corrosion-erosion protection

Jorge Morales Hernández[1], **José Manuel Juárez García**[2], **Héctor Herrera Hernández**[3], **Héctor J Dorantes Rosales**[4] **and Raul Herrera Basurto**[5]

[1] Centro de Investigación y Desarrollo Tecnológico en Electroquímica S.C., Parque Tecnológico Querétaro s/n, Sanfandila, Pedro Escobedo, Querétaro, C.P. 76703, Mexico
[2] Universidad Tecnológica de Querétaro, Av. Pie de la Cuesta 2501, Nacional, 76148 Santiago de Querétaro, Mexico, C.P. 76148, Mexico
[3] Universidad Autónoma del Estado de Mexico, Lab. de Electroquímica Aplicada, Blvd. Universitario s/n, Atizapán de Zaragoza, Estado de Mexico, 54500, Mexico
[4] Instituto Politécnico Nacional, Escuela Superior de Ingeniería Química e Industrias Extractivas (ESIQIE), Av. Instituto Politécnico nacional s/n, Lindavista, Gustavo A. Madero, C.P. 07738, Ciudad de Mexico, Mexico
[5] Instituto Tecnológico de Morelia (TecNacMex), Depto de Investigación y Posgrado, Avenida Tecnológico 1500, 58120 Morelia, Mich., Mexico

E-mail: jmorales@cideteq.mx

Keywords: high-temperature coatings, wear and corrosion protection, Ni-Ti-B ternary system, geothermal corrosion protection, metal-ceramic phases

OPEN ACCESS

RECEIVED
27 September 2021

REVISED
30 November 2021

ACCEPTED FOR PUBLICATION
1 December 2021

PUBLISHED
15 December 2021

Abstract

Significant contribution on corrosion-erosion resistance of Ni_3B-TiB_2 nanocomposite coating of 1 μm of thickness, deposited by DC magnetron Sputtering on stainless steel 304 substrates was studied. Nickel phase (γNi) plus Ni_3B-TiB_2 phases were synthesized previously by Mechanical Alloying (MA). Solid cathode (76.2 mm of diameter and 3 mm of thickness) used to grow thin films was manufactured with the alloyed powders, applying a uniaxial load of 70 MPa at room temperature and sintered at 900 °C for two hours. Microstructure and mechanical properties of the coatings were characterized by x-ray diffraction (XRD), scanning electron microscopy (SEM), atomic force microscopy (AFM), nanoindentation, and wear test with a ball-on-disc tribometer. Compact coating of Ni_3B-TiB_2 with a microstructure of prismatic crystals after annealing treatment, showing a uniform coating with good adherence and low friction coefficient of 0.5, correlated with a low roughness of $Ra \approx 0.0439 \pm 0.0069$ μm. The average hardness of 537.4 HV (5265.0 MPa) and wear coefficient at room temperature of 2.552E-10 m^2N^{-1} correspond with medium-hard phases with an elastic-plastic behavior suitable for fatigue applications. Geothermal fluid modified was synthesized in the lab with $NaCl/Na_2SO_4$ to evaluate the corrosion resistance of the films in a standard three electrodes cell, characterizing a corrosion rate of 0.0008 and 0.001 mm^*year^{-1} at 25 and 80 °C respectively during 86.4 ks (24 h) of exposition; showing a resistive coating without corrosion products and with good response to the geothermal environment.

1. Introduction

1.1. The importance of metal-ceramic materials

The combination of Corrosion-erosion is a primary form of failure that causes disasters and significant financial losses to the power generation industry. High-Temperature Ceramics (HTCs), such as borides, carbides, and nitrides, are considered possible to synthesize materials for use in extreme environments. By their high hardness, thermal and chemical stability, ceramic coatings are widely used as protective coatings in high-temperature components; however, the high brittleness and low toughness limit their industrial applications under fatigue and corrosion conditions [1].

Metal-ceramic materials (MCM) are considered a functional alternative by their high mechanical and chemical stability versus the temperature increase under a corrosive environment, so it is possible to increase the

corrosion-erosion resistance of the power generation components using metal-ceramic materials with the appropriate combination.

The high melting temperature, thermal conductivity, elastic-plastic behavior, resistance to erosion, and corrosion make metal-ceramic materials suitable for high-performance applications [2].

Most of the interactions between Group 4 diborides and transition metals, e.g., nickel, are poorly known or not known at all. Given these potential applications, it is then necessary to investigate, in addition to the individual properties of these materials, their interactions in some combinations between TiB_2 and Ni_3B phases to determine their capacity to offer corrosion-erosion protection [3].

The research and development of functional coatings of new metal-ceramic materials using a new route of processing that combines Mechanical Alloying and PVD Sputtering offer great possibilities for protecting components exposed to aggressive environments where the wear and corrosion at high temperature are the leading root cause of failures.

1.2. Geothermal corrosion and erosion

Generation of electrical energy needs the use of steam in different processes such as thermoelectric and geothermal units; however, steam is highly erosive due to the presence of solid particles of different shapes and sizes, as well as highly corrosive due to the presence of silicates, carbonates, sulfates, chlorides among other compounds, with pH values in the range of 6 to 8. Among the different corrosion mechanisms to which a generation turbine is exposed, and particularly the components such as rotors, discs, blades, connections, and other components made of SS304, the most common are stress-corrosion cracking (SCC), followed by pitting corrosion (P), corrosion fatigue (CF), accelerated flow corrosion (FAC) and corrosion-erosion.

Geothermal reservoirs can classify as low (40 °C–90 °C), medium (90 °C–150 °C), and high-temperature (150 °C and upper) reservoirs, being, for the moment, the low-temperature geothermal reservoirs of our interest, working to the temperature of 80 °C under a corrosive medium with chlorides and sulfates. In this context, the protection of turbine components to increase their life and reduce catastrophic failure requires advanced coatings of corrosion-erosion protection.

1.3. Relevancy of the TiB_2 and Ni_3B phases

TiB_2 ceramic is considered an advanced engineering ceramic due to its excellent physical, chemical, and mechanical properties such as high melting point, high hardness, high Young´s modulus, good corrosion resistance, and excellent electric conductivity. TiB_2 is an excellent refractory phase, with applications in crucibles as a thermal barrier, neutron absorber, catalytic electrodes, cutting tools coating, corrosion-erosion protection, and other applications [4].

TiB_2 is commercially synthesized by carbothermal reduction process (CRP), using TiO_2 with B_2O_3 or B_4C at high temperature, followed by rapid quenching; however, this method has reported complications to obtain an ultrafine grain, with a negative effect on their physical properties. The endothermic reaction needs a high energy consumption that represents a high cost and reduces the possibility of considering the CRP as a process for large-scale production, together with other environmental implications [5]. TiB_2 is a compound with both ionic and covalent bonds, which demand very high temperature during the solidification process, so the grain growth rate of TiB_2 is rapid, and as a consequence, it is not very easy to obtain a pure and ultrafine-grain, harming the properties of TiB_2 [3, 5].

On the other hand, Ni-alloys with additions of B are attractive for high-temperature applications. These alloys effectively improve the mechanical properties of ceramic compounds, particularly the brittleness compared to the addition of pure Ni. Thermodynamic calculations for the Ni-B-X (X = Ti, Zr, HF) ternary systems demonstrated that alloying of Ni with B effectively reduces and even suppresses the dissolution of transition-metal diborides [6].

Ni_3B phase is of great interest in energy, catalysis, and optics with good electrocatalytic activity, concerning the standard Ir/Ru compounds [7]. In this research, the Ni_3B phase reduces the high hardness of the TiB_2 phase with the capacity to offer corrosion-erosion protection in a metal-ceramic material balanced.

The attractive physical and chemical properties of metal-ceramic material make the Ni-Ti-B system attractive for high-temperature applications, particularly for the presence and combination of the TiB_2 and Ni_3B phases [8, 9].

A complex transformation in the Ni-Ti-B ternary system is required to synthesize the TiB_2 (H-boride) and Ni_3B (O-boride) phases. While the nickel phase (γ-Ni) is present, the TiB_2-Ni_3B phases can be nucleated by thermal activation inside this (γ-Ni) phase [10, 11]. The rapid heat transfer during the solidification can be reflected in more nucleation and growth of the Ni_3B (O-boride) phase, with high residual stresses and the subsequent formation of cracks [12].

1.4. Mechanical alloying for the synthesis of metal-ceramic materials

Mechanical Alloying is an economical technique for synthesizing glassy metals in the solid-state concerning the traditional melting and rapid solidification [13]. MA has been a successful one-step route to synthesizing refractory compounds like borides, carbides, and nitrides. This technique offers the possibility of synthesizing amorphous phases, intermetallic compounds, and hardened materials, with the chance to expand the synthesis to glassy metals [14]. This process is not only capable of reducing grain size; it can also modify the crystalline structure with more symmetry due to the more disordering of the punctual and lineal defects at the crystalline lattice [15].

Synthesis by MA of intermetallic compounds with Ni matrix has reported the formation of NiAl, Ni_2Al_3, and a metastable solid solution of Al in Ni. NiAl intermetallic compound by MA was reported in the range of 25 to 65 at% of Ni, whereas the equilibrium range goes to 46 to 59 at% of Ni, assuming that contamination with iron from the milling media is the catalyst to extend the solubility limits [16].

$Ni_{60}B_{40}$ and $Ni_{80}B_{20}$ compositions milled in a planetary ball mill after 198 ks (55 h) of milling showed the formation of the Ni_2B tetragonal with high boron content and Ni_3B orthogonal with low boron content [6]. TANG Wen-ming *et al* [9] reported the synthesis of TiB_2 nanocrystalline powder by MA from the composition Ti-67B (mole fraction, %). With 216 ks (60 h) of milling, only TiB_2 was detected with a crystal size in the order of 10 nm. With thermal activation, TiB_2 was a stable phase and with a minimum grain growth.

Preliminary studies in the mechanochemical synthesis of the Ni-Ti-B ternary system reported the stable formation of the Ni_3B- TiB_2 phases with the increase in the titanium content after 86.4 ks (24 h) of milling. The transformation sequence controlled for diffusion and thermal activation is represented in reaction 1 [8].

$$\begin{aligned} &\mathrm{Ni} + \mathrm{Ti} + B \xrightarrow{24\ h\ \text{of MA}} f.c.c.(\gamma\ \mathrm{Ni}) \\ &+ \mathrm{TiB_2} + \mathrm{Ni_2B} + Ni_3\mathrm{B} + \xrightarrow{\Delta} \mathrm{Ti}B_2 + \mathrm{Ni_3B} \end{aligned} \tag{1}$$

The combination of TiB_2 with other phases of less hardness and with an elastic-plastic behavior like the Ni_3B phase has demonstrated get a balance between the hardness and toughness properties of the mixture synthesized by *MA*; being the control in the grain size, the stability of phase transformations and the minimum process energy the main aspects to selecting MA for the synthesis of this composite material [8].

The Physical Vapor Deposition Process is an evaporation technique to synthesize thin films of high density and with a minimum porosity in the order of nanometers. With this technique, the coating conserves the chemical composition from the cathode (compacted from the mechanically alloyed powders) with a nanocrystalline structure and good mechanical and chemical properties [17].

TiB_2-Ni_3B phases has been few reported because the synthesis of each phase is complex and unstable under the conventional processes [1].

This research has the perspective of establishing the bases in the state-of-the-art about the advanced surface treatment across the growth of TiB_2-Ni_3B composite coatings for corrosion-erosion protection.

2. Experimental details

2.1. Target manufacturing

Previously, the phases TiB_2 and Ni_3B were synthesized by Mechanical Alloying from elemental powders of Ni, Ti, and B of high purity (99.7, 99.5, and 99.3%, respectively) with the composition of Ni_{60}-Ti_{30}-B_{10} (wt%). The powders were milled for 24 h under an inert atmosphere in a high-energy system mark SPEX, model 2000. The alloyed powder was compacted with a uniaxial pressure of 70MPa and sintered at 900 °C for two hours in an inert atmosphere to obtain a solid target of 76.2 mm of diameter and 3mm of thickness. Structural change of the cathode before and after sintering was characterized by x-ray diffraction (XRD) in a diffractometer mark Bruker; model D8 advanced with Cu-Kα ($\lambda = 1.542$ Å). JADE software from The International Center for Diffraction Data was used to identify the 2θ positions of the diffraction peaks, and the validation of the TiB_2 and Ni_3B phases after the sintering process was characterized by Transmission Electron Microscopy mark Jeol, model 2000.

2.2. Synthesis of coatings and physical characterization

Stainless steel 304 (SS 304) substrates of square dimensions (50 mm × 50 mm) were desbasted with a silicon-carbide paper of different grades and were polished with a diamond-based suspension of 1μm of particle size until getting a mirror surface. After polishing, the samples were cleaned with liquid soap and degreased with acetone. Hot air dry was used before putting the substrates into the PVD reactor for the growth of films. TiB_2-Ni_3B thin films were deposited by reactive DC magnetron sputtering in a semi-industrial PVD reactor during 70 min of growth, at 60 °C of the temperature inside the chamber and 150 W of power. During the

process, argon and nitrogen flows were of 30 and 14 sccm, respectively. The initial pressure in the chamber was below 3.0E−3 Pa, while the deposition pressure was in the order of 1.8E−2 Pa. The coatings were annealed at 300 °C for 0.5 h in an electric furnace with a vacuum atmosphere to promote crystallinity, the diffusion between particles, and reduce the nanoporosity.

The thickness of the coating was characterized in a cross-section of the coating mounted in conductive bakelite and characterized in a Jeol, JSM 6460 Scanning Electron Microscopy. The Glow Discharge Spectrometry technique (GDS) was used to know the composition profile of the coating from the surface to the core, using the HORIBA Scientific equipment, model GD-Profiler 2 with 35 W of power, and a depth resolution of 1 nm.

The topography of the coating surface was characterized with a high-resolution scanning electron microscope (Field emission-SEM), mark HITACHI, and atomic force microscope in contact mode with an equipment FISHER, Nanosurf Nanite AFM, and C3000 Control Software. The structure of the films was evaluated by x-ray diffraction (XRD) in a diffractometer mark Bruker; model D8 advanced with Cu-Kα ($\lambda = 1.542$ Å). A scan mode detector and with an incident angle of two grades were used [16]. Nanoindentation measurements on the coating surface were performed on the FISHER machine, model Picodentor HM500, with a diamond pyramid-shaped Berkovich V type, indenter DIA H2N. The cyclic nanoindentation test applied 3 and 4 mN of load with an application time of 20 s divided between the load and unload, and the indenter was held 5 s of creep at 15% of the maximum load for thermal drift corrections.

Wear testing at room temperature was performed on a CSM Instrument, ball-on-disc tribometer in five coated samples. Stainless steel hardened sphere of 5 mm in diameter was used as a counter to print a circle in 10 mm of diameter until a total distance of 288 m. The test parameters were a constant rotation speed of 200 r min^{-1}, a normal load of 5 N, relative humidity of 36%, and without lubrication (dry sliding). The friction coefficient was recorded during all the distances of the test [17].

2.3. Corrosion evaluation

The corrosion test was performed in samples coated and annealed, using an electrochemical cell with a typical configuration of three electrodes at 80 °C for 24 h of exposition. The coating was used as the working electrode (WE) with a normalized area of 1 cm2, a stainless steel bar was the counter electrode, and a saturated calomel electrode (SCE) was used as a reference electrode. The SS304 is drastically affected by chlorides and sulfides at a temperature above 60 °C, which is why it is seriously damaged by geothermal fluid of low temperature. Under this condition was proposed to use an electrolyte composed of NaCl-Na_2SO_4 with a concentration of 0.28 M (NaCl) and 0.01 M (Na_2SO_4), prepared with reagent grade salts and distilled water in laboratory conditions. Linear polarization resistance technique (LPR) was implemented to obtain the corrosion potential (Ecorr), corrosion current density (jcorr), and the Stern-Geary coefficient (B). Polarization curves were recorded every eight hours until a total of 24 h with an over-potential of ±250 mV and speed of 0.166 mV s^{-1}. The corrosion rate was determined by obtaining Linear fits with the UiECorr software for corrosion research with BioLogic Instrumentation. Finally, the corrosion mechanism on the affected surface was evaluated with an optical microscope.

3. Results and discussion

3.1. Target characterization

The XRD pattern corresponding with the compacted target is shown in figure 1(a), where the TiB_2, Ni_2B, and Ni_3B phases were characterized together with the Ni phase (γ-Ni); this last one corresponds with the solid solution of Ti and B into Ni structure.

After the sintering of the target (figure 1(b)), the γ-Ni and Ni_2B phases were dissolved and transformed, respectively, allowing more boron diffusion to complement the formation of Ni_3B and TiB_2 phases [18]. This thermal activation promoted the nucleation and growth of Ni_3B and TiB_2 as equilibrium phases [19].

TiB_2-Ni_3B phases were confirmed after the sintering process with the diffraction patterns obtained by TEM. The bright-field micrograph in figure 2(a) with its corresponding selected area indexed diffraction pattern shows small black particles that belong to the TiB_2 phase with a zone axis in [1120]. Figure 2(b) shows a significant white particle corresponding to the Ni_3B phase with a zone axis [011]. Figure 2 shows that the Ni_3B phase corresponds with the matrix and the TiB_2 phase is the reinforcing particle, so the physical and chemical properties of the composite are defined by the Ni_3B phase and complemented with the TiB_2.

Has been demonstrated that the presence of Ni compounds, reduces the hardness and stabilizes the formation of the nanoparticles of TiB_2 at high temperatures [12, 20]. The presence of Ni_3B has permitted the uniaxial powder compaction during the manufacturing of the cathode due to their high ductility and, has improved the TiB_2 phase stability during the sintering; improving the mechanism of solid-state diffusion to

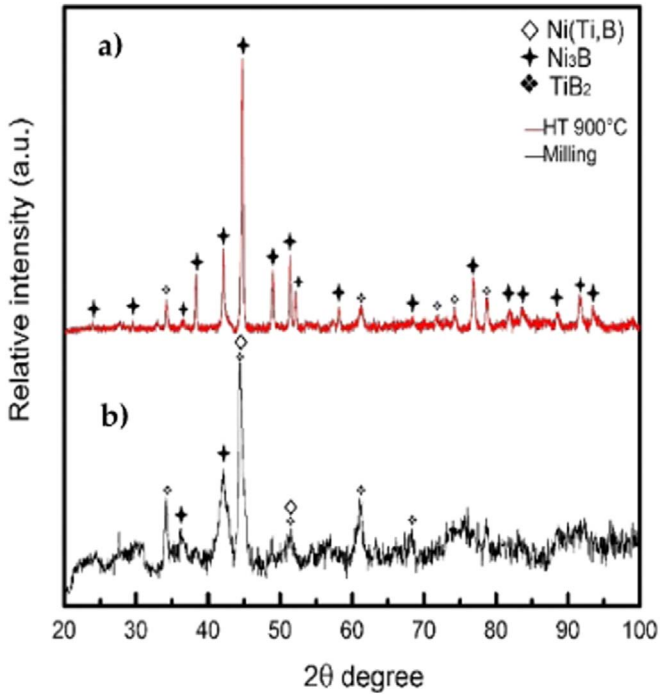

Figure 1. X-ray diffraction patterns of (a) milled powders at the maximum milling time and (b) cathode after sintering at 900 °C.

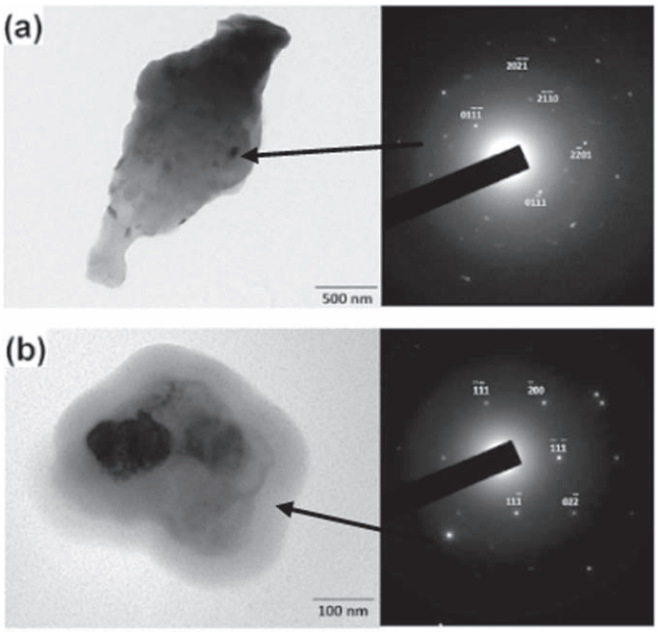

Figure 2. Transmission electron micrographs of the cathode with its corresponding diffraction pattern from the (a) TiB_2 phase in [1120] and (b) Ni_3B phase in [011].

obtain a densified cathode (9.75 g cc^{-1}.) and conserving the crystal size for the continues deposition of TiB_2-Ni_3B thin films by DC Magnetron Sputtering.

3.2. Sputtered thin films

3.2.1. XRD characterization

The coating characterization by XRD shows the presence of the characteristic peak corresponding with TiB_2 (1010) and Ni_3B (220) as the main phases (figure 3), according to the XRD results from the cathode. The addition of N_2 as a reactive gas promoted the formation of metallic nitrides to increase the coating hardness without increasing the residual stress in the sputtered film [21, 22].

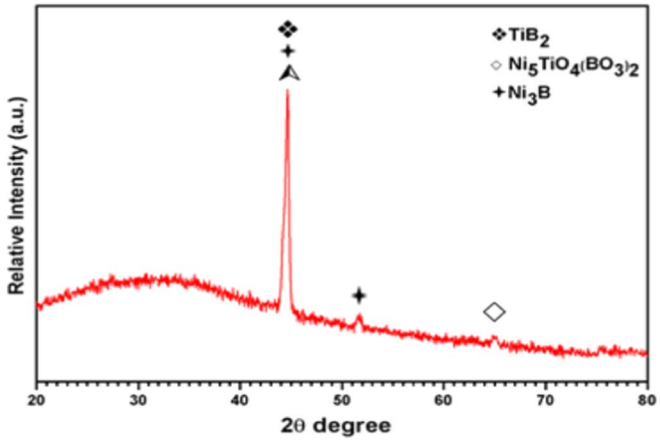

Figure 3. X-ray diffraction pattern of sputtered TiB_2 –Ni_3B thin film with scan mode.

The formation of metallic nitrides depends on the reactivity of the deposited compounds during the evaporation; however, these were not characterized in the coating diffraction pattern due to the excellent stability of the Ni_3B and TiB_2 deposited phases (figure 3). Microcracks at the surface were not detected due to the low residual stresses on the film obtained with the complete recrystallization of the phases [23]. Independent that the formation of metallic nitrides was not possible, the appearance of the coatings is good with no possibility of detachment.

3.2.2. Surface characterization

PVD process involves the physical ejection of material (atoms or molecules), condensation, nucleation, and growth onto a substrate where the microstructure of the film can be periodic, have a set pattern, or be entirely random; this depends primarily on the energy of the species (adatoms) incident upon the substrate. Likewise, the incidence angle can affect the adatoms and affect the micro or Nano porosity of the coating [24]. Surface characterization by high-resolution SEM (figure 4) shows a random particle deposition with a particle size distribution in the order of nanometers.

Figure 4(a) shows a uniform dispersion of nanometric particles with a semi-spherical geometry and superimposed on the surface, with perception as they have not adhered to the substrate. Figure 4(b) shows a distribution of particle size in the order of 100 nm or less, and figure 4(c) shows that the distance between particles is less than 100 nm, identifying the formation of some diffusion necks between particles which can promote de reduction of the nanoporosity by the effect of the temperature during their exposition to the geothermal environment.

To reduce the particle size dispersion deposited at the coating is recommended to modify the deposition parameters like power, argon flow which modify the plasma kinetic, power source type, the temperature inside the chamber, the distance between cathode and substrate, etcetera; all of them applied to modify the deposition rate and improve the coating densification. For example, P Sigmund indicated that the sputter yield (Y) value is inversely proportional to the bond energy (Us) from the cathode´s surface, as is shown in equation (2) [25]. If the surface´s bond energy to pull an atom changes from the cathode surface to the core (density profile), this condition can result in variations of the deposition rate, promoting changes in the morphology and size of the deposited particles.

$$Y = \frac{3}{4\pi^2}\alpha\frac{4M_1M_2}{(M_1+M_2)^2}\frac{E}{U_s} \tag{2}$$

where:

E is the projectile´s energy.

M1 and M2 are the projected atom mass and target atom mass (amu).

Us is the surface bond energy.

α is a dimensionless parameter that depends on the mass ratio and ion energy.

Surface characterization of the thin films after deposition by AFM shows a pattern consisting of conglomerate particles in a continuous arrangement (figure 5(a)) consistent with the SEM micrographs. In the progression of the dimensionality of thin films, this type of growth is classified as 0D quantum well (quantum dots) with widths between 3 and 10 nm [26]. The images by AFM show a minimum surface roughness with an

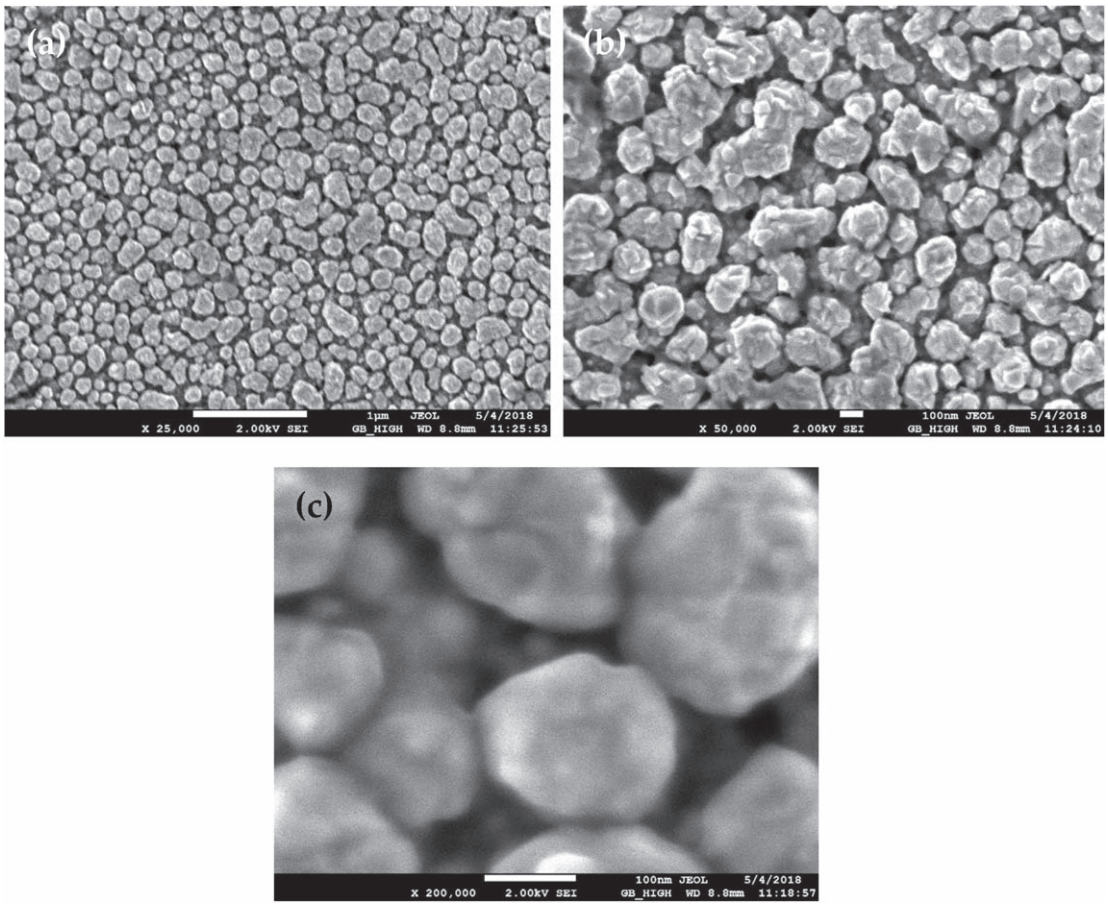

Figure 4. High-resolution surface morphology of Ni_3B–TiB_2 thin film at different magnifications; (a) 25,000 X, (b) 50,000 X and (c) 200,000 X.

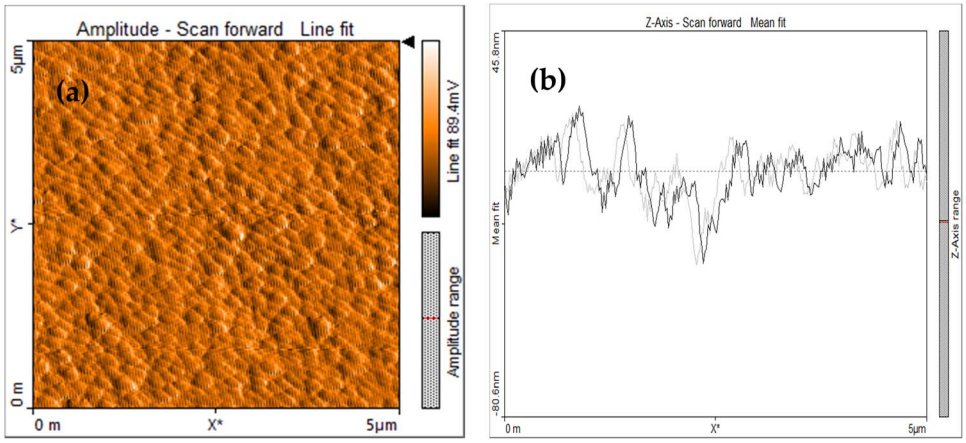

Figure 5. AFM topography images of Ni_3B–TiB_2 coating after deposition. (a) conglomerate particles and (b) surface roughness.

average value of 0.0439 $\pm$ 0.0069 μm in the Ra scale according to the profiles shown in figure 5(b). This low roughness typical of PVD coatings reduces the friction coefficient, increasing the lubricant behavior and the fatigue life.

The annealing heat treatment to the coating has favored the nucleation and growth of prismatic crystals overlapping with redounded borders, reducing the interconnected nanoporosity at the surface (figures 6(a) and (b)), with a surface of smooth appearance. However, the surface profile shows an increase of roughness in the order of hundreds of nanometers to 196.5 μm, which could affect the functionalization of the coating under load and wear conditions.

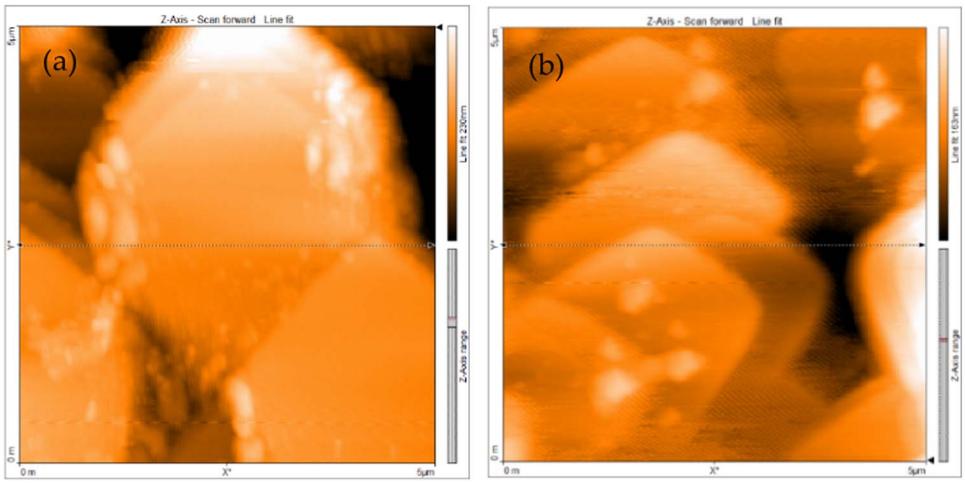

Figure 6. After nucleation and growth, AFM topography images of (a) and (b) prismatic crystals from the Ni_3B–TiB_2 coating after the annealing treatment.

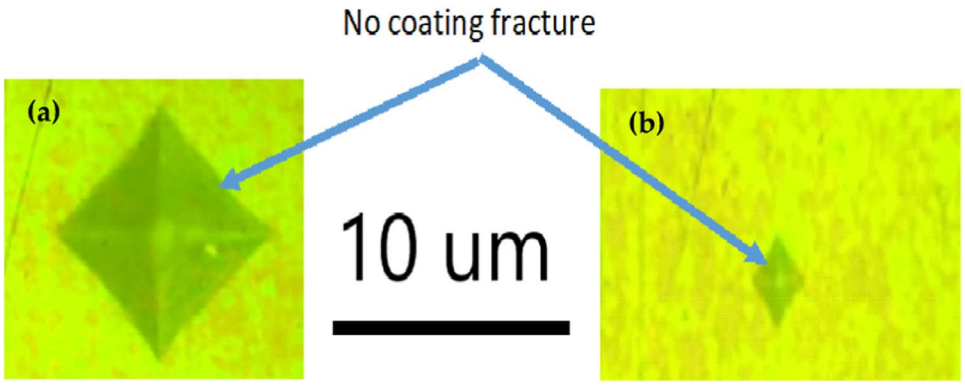

Figure 7. Vickers indentations with (a) 1000 and (b) 100 gf of load respectively on Ni_3B - TiB_2 coating.

3.2.3. Adherence coating and thickness

In evaluating the quality of work involved in coatings application, skills and knowledge of the coating technique apply different standards [27]. The adhesion of coatings is determined as the coatings are not fused to the substrate and are very dependent on surface preparation prior to deposition. The most common approach to determine coating adhesion is to measure the tensile load needed to detach the coating from the substrate in coatings with thickness over 250 μm according to the ASTM standard C633–13. An alternative approach allows measurement of coating adhesion on flat plate specimens with an apparatus known as pull-off adhesion tester according to ASTM standard D 4541 −02. However, when the coating has 1 μm of thickness or less, the last two methods are not applied. The empirical method using Vickers indentation defines the adherence of thin films when some delamination around the border of the pyramidal mark is observed in function of the applied load. Figure 7 shows the Vickers marks with 1000 and 200 gf of load, respectively, where the fracture of the coating at the border of the pyramid mark was not observed as an indication of the excellent adherence of thin films. If a film fracture at the edges of the pyramid mark is evident, this is a failure condition for poor compliance. In this case, the Ni_3B-TiB_2 coating exceeded 1000 gf of load without fail.

Scanning electron microscopy was used to measure the coating thickness in a cross-section of the sample mounted in conductive Bakelite. The coating thickness measured was 1 μm, as shown in figure 8, which is characterized as a compact coating with a uniform thickness, where the interphase with the substrate does not show porosity or separation between the coating and substrate, confirming that the coating has good adherence at the substrate [28]. The glow discharge surface (GDS) technique generates a plasma that produces an erosion in a coating and quantifies the chemical composition concerning the coating depth. If the coating thickness measured was 1 micron, we can see (figure 9) how the concentration of titanium and boron near the substrate tends to increase towards the surface and decrease near the surface of the coating (cero depth). Ideally, the deposition rate of nickel will be more than titanium and boron because it corresponds with the matrix, and the

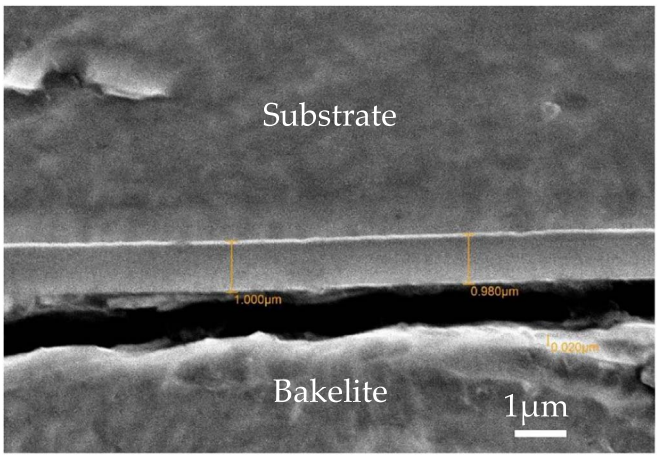

Figure 8. The coating thickness of Ni_3B-TiB_2 coating in a cross-section.

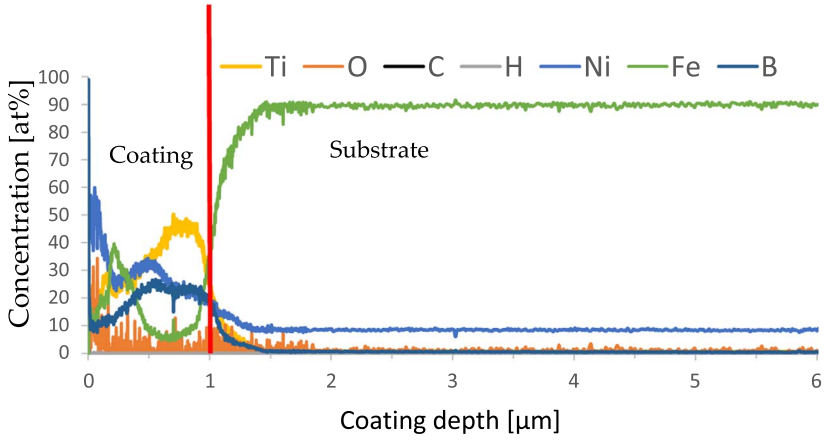

Figure 9. Compositional depth profile of Ni_3B -TiB_2 coating by GDS.

relations Ni/B and Ti/B tend to increase from the substrate and toward the coating surface to maintain the stability of the Ni_3B and TiB_2 phases.

3.2.4. Coating hardness

There are not enough reports about mechanical properties of the TiB_2–Ni_3B system, however, high hardness values have been reported for TiB_2-Co alloy, in the order of 1777 HV (17430 MPa), and some boride compounds have reported hardness over 700 HV (6865 MPa) [29, 30].

TiB_2–Ni_3B coating hardness reported an average value of 537.4 HV (5265.0 MPa); not as high as reported for the TiB_2 phase, more significant than 1000 HV [29]. The hardness coating shows the contribution of the Ni_3B phase in the reduction of TiB_2 hardness, with an elastic-plastic behavior as is shown in the load-displacement curves in figure 10 and that corresponding with a crystalline material, which can withstand fatigue conditions (thermal and mechanical) without becoming fragile. The coating hardness was two times higher than the uncoated substrate (256 HV (2511 MPa), within the typical hardness range required for wear conditions.

A few increases of the boron content in the mixture (in the order of 30 wt%) to synthesize the composition Ni_{40}-Ti_{30}-B_{30} should increase the percentage of the TiB_2 phase concerning the Ni_3B, increasing the hardness and having a super-hard coating, with and a light elastic-plastic behavior due to the Ni_3B presence as the second phase [31].

The average depth during the nanoindentation test was 0.134 μm with 3mN of load (figure 10). Were discarded measurements with 4mN of the load because the load-displacement curves show pop-in events characteristic of brittle solid, including the substrate effect in the hardness. The coating's hardness is inside the range of medium-hard materials for industry applications (537.4 HV). The contact under load and abrasive conditions are possible because it does not correspond with a brittle material. The increased roughness after

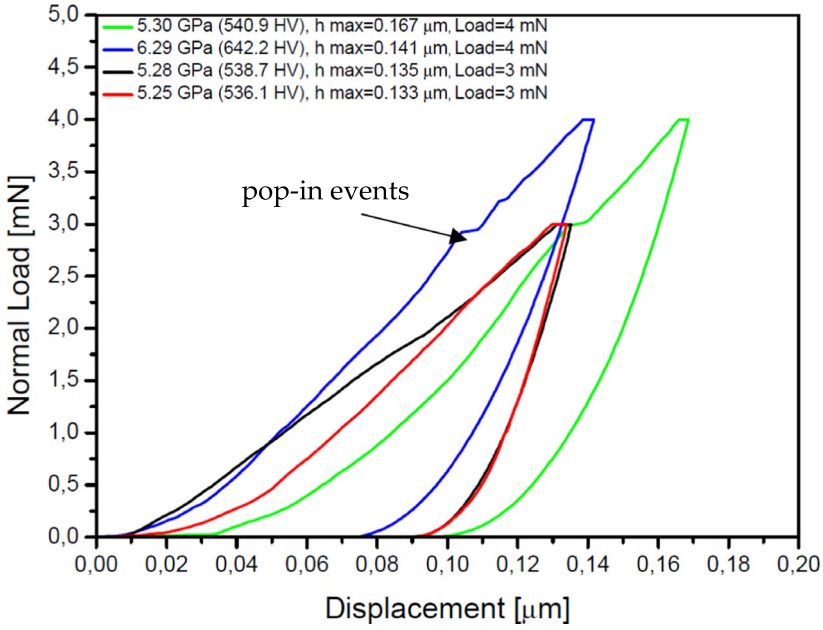

Figure 10. Load-displacement curves of the TiB_2-Ni_3B coating with 3 and 4 mN of load.

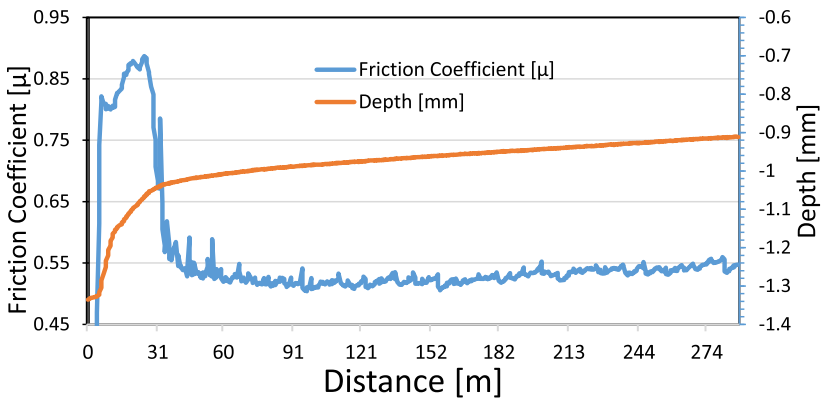

Figure 11. The Friction coefficient and wear depth versus displacement of the wear test with 5 N of load on the TiB_2 -Ni_3B coating.

annealing could be another factor that affected the contact of the Berkovich indenter during the displacement, producing these pop-in events.

3.2.5. Wear test

The wear resistance of protective coatings is expressed in terms of their ability to resist abrasion without fracturing. A typical wear test involves monitoring wear depth and the record of friction coefficient against standard wear distance. Figure 11 shows the transition from the elastic to plastic deformation on the coating, indicating a slope change in the friction coefficient at 50 m of travel. The reduction of friction coefficient from the start point was progressive with the material compaction and alignment of the crystals, corresponding with the change from abrasive to adhesive wear of the coating, characterized by the accumulation and transfer of material from one surface to another along with the wear test [32]. The average friction coefficient during all the traveling (288 m) was 0.5, considered this value characteristic of a dry sliding material [33]. No micro-cracks, pitting, and spalls, or substrate exposition were observed in the wear mark. SEM characterization of the wear mark confirms the adhesive wear as a failure mode, represented by the wear mark in figure 12.

A profilometer topographically measured the volume loss for the calculation of wear rate. The Ka wear coefficient calculated for the TiB_2 -Ni_3B coating was 2.552E-10 $m^{2*}N^{-1}$, which is higher concerning the wear rate of nitride hard coatings by PVD (1E-14 $m^{2*}N^{-1}$); nevertheless, it is better than the uncoated SS304 with a wear coefficient of 3.47E-3 $m^{2*}N^{-1}$. The wear rate of the Ni_3B - TiB_2 coating corresponds with their hardness of 537.4 HV, which was better also than the uncoated SS304 of 265 HV.

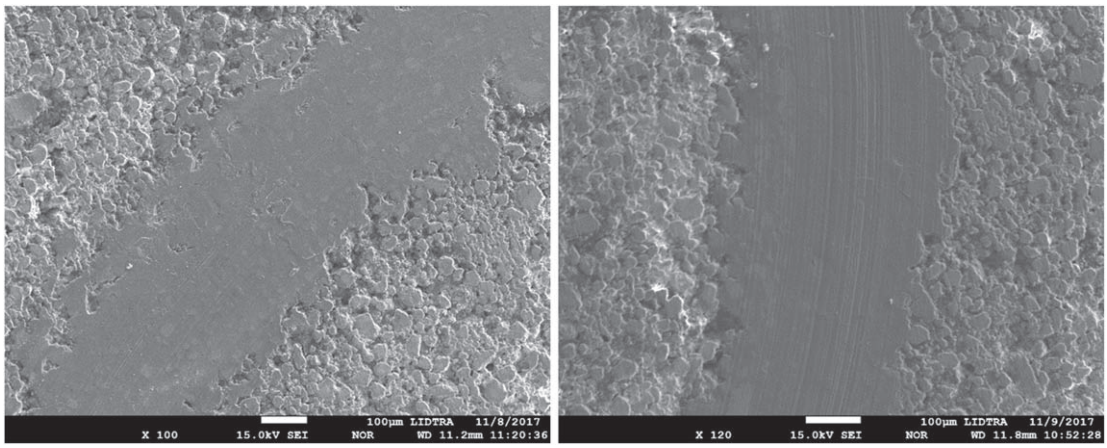

Figure 12. Wear mark at different positions after 288 m of displacement.

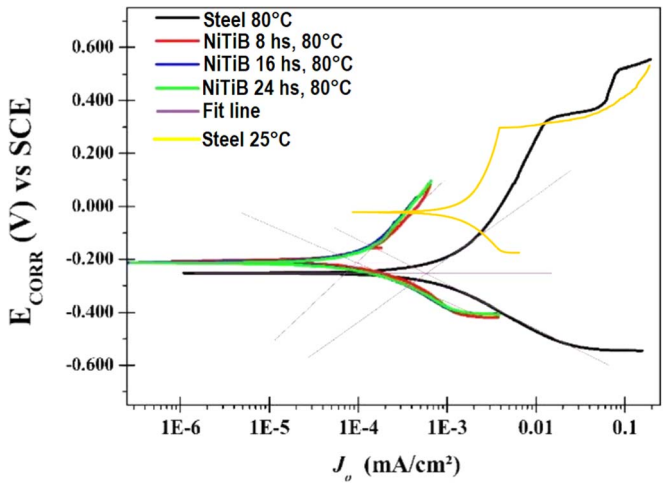

Figure 13. Polarization curves at different exposition times in NaCl/ Na_2SO_4 at 80 °C.

3.3. Electrochemical evaluation

Typically, the Ni and Cr are considered high corrosion resistance elements and are essentials in the SS. The high content of Cr reduces the mechanical properties at the high temperature of the alloyed steels, so replacing it with an austenitic element like nickel improves the thermofluency [34]. Titanium has good corrosion resistance and good mechanical properties at high temperatures; however, alloying elements in SS in moderate concentration are not convenient. Ni_3B - TiB_2 composite coating shows good thermal stability at high temperatures, offering excellent corrosion and wear resistance to the steel substrates.

There are significant differences in the mechanical and chemical behavior of traditional metals concerning nanocomposites or nanocrystalline arrangements [35]. The corrosion rate of SS304 increased from 0.0032 mm*year-1 to 0.0067 mm*year-1 when the temperature changed from 25 to 80 °C (figure 13). The result corresponds with the increasing current density and the displacement toward more negative E_{corr}. If the temperature increases to 120 °C that corresponds with the medium temperature of Geothermal reservoirs, the corrosion rate for the SS304 increases exponentially until 33.772 mm*year^{-1}[34]. This increase of corrosion rate of the SS304 with the temperature is possible when the passive behavior of the anodic reactions of the steel is unstable, or the passive response of the material does not protect the base metal under these environmental conditions.

Polarization potentials are generally time-dependent and represent the evolution of the corrosion reactions [36]; however, the coating's cathodic and anodic polarization curves after 8, 16, and 24 h of exposition were similar. It could be said that corresponding with the same electrochemical reaction independent of the exposition time due to the chemical stability of the coating; in such a way that in each time interval, the curves overlapped as if the same corrosion reaction is repeated without progressive material degradation [37, 38].

Table 1. Corrosion rate at 80 °C in function of time of PVD coatings.

Sample	Ecorr versus SCE (mV)	B (V)	Icorr (A · cm^{-2})	Corrosion rate (mm· year^{-1})
SS 304	−255	0,0473	6,48E-07	0,0077
TiB_2-Ni_3B 8h	−206	0,0378	8,80E-08	0,0010
TiB_2-Ni_3B 16h	−212	0,0431	8,50E-08	0,0010
TiB_2-Ni_3B 24h	−214	0,0401	8,50E-08	0,0010

Table 2. Corrosion rate at 25 °C in chloride medium of different coatings and process.

Sample	Process	Ecorr versus SCE (mV)	I corr (A·cm^{-2})	Corrosion rate (mm·year^{-1})
SS 304	—	−32,174	3,06E-07	0,0036
SS 316	—	−284	5,290E-07	0,0063
Ni_3B-TiB_2	PVD	−180	6,88E-08	0,0008
TiN	PVD	99	5,30E-07	0,0063
TiCN	PVD	73	5,08E-08	0.0006
CrNi	HVOF	−180	9,10E-07	0.0108
NiCr	HVOF	−270	2,65E-07	0,0031

When uniform corrosion occurs, the passive layer or the coating will be destroyed progressively until activating the substrate surface, increasing the corrosion rate with time. On the other hand, in strongly oxidizing environments with hot chlorides and sulfides, the passive layer from stainless steel, when it is not stable, shows localized corrosion like pitting and crevice, with a displacement of the polarization curves with the time and temperature. In this case, the resistivity of the coating is stable, and the possible oxidized soluble species produce an effect called transpassive corrosion without displacement of the polarization curves.

Results reported in table 1 show that the corrosion rate of the coating is the same order of magnitude in the function of time and constant temperature, and the resistivity is six times higher on average concerning the substrate.

The chemical composition and consistency of the coating are fundamentals for maintaining their corrosion resistance [39]; for example, the thermal spray technique of High Velocity of oxy-fuel (HVOF) is used for deposition of coatings in the solid-state of commercial materials for the protection of vapor turbines. This technique has limited usefulness in the deposition of corrosion protection coatings due to the presence of interconnected porosity in the structure of the coatings, requiring in some cases the application of a post-treatment of sintering process to reduce the interconnected porosity with the implications of the base metal deformation. The corrosion rate at room temperature of the coatings deposited by HVOF was similar to the uncoated stainless steels (SS304 and SS316) without improving the corrosion protection. The Ni_3B - TiB_2 and TiCN coatings deposited by PVD offered better corrosion protection for the stainless steels due to their metal-ceramic behavior, more resistivity, and consistency. The corrosion rate at room temperature of high Cr and Ni coatings deposited by HVOF together with the Ni_3B - TiB_2 coatings deposited PVD are shown in table 2.

The few variations in these parameters indicate that the coating was not sensitized with the exposition time and temperature, showing its stability to chemical attack. The anodic curves did not exhibit self-passivation behavior, which shows that the corrosion resistance of coating does not depend on the formation of a passive film or corrosion products that promote the protection of the coating. The coating can exhibit a resistive behavior, which reduces the transfer of electric charge and maintains a constant corrosion rate with the exposure time.

Delamination of the coating was characterized by optical microscopy after 24 h of exposition (figure 14), showing generalized corrosion as a failure mechanism. The nanoporosity at the coating permitted the permeation of the electrolyte, so it is possible to modify some deposition parameters that change the growth rate and coating roughness to improve the coating densification.

Tests samples of 50 × 50 mm with the Ni_3B-TiB_2 coating were exposed for one month at the direct flow of a geothermal fluid at the unit Los Humeros, Mexico (figure 15). After their exposition, the coating did not show corrosion products at their surface, and no substrate degradation did observe. Some discoloration of the coating was observed without damage by the erosion of the geothermal environment. The opposite side of the test sample that corresponds with the uncoated SS304 (substrate) shows the deposition of salts with the characteristic yellow color of sulfurs and the withe color of chlorides. For the deposition of salts is necessary first the general corrosion or pitting of the substrate. That demonstrates the vulnerability of SS304 in this geothermal environment.

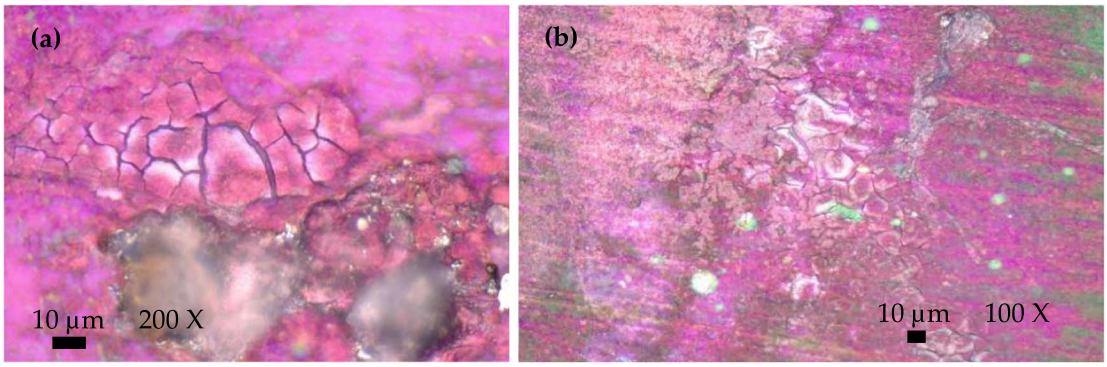

Figure 14. Optical micrograph at (a) 200X and (b)100X after 24 h of exposition in $NaCl/Na_2SO_4$ at 80 °C.

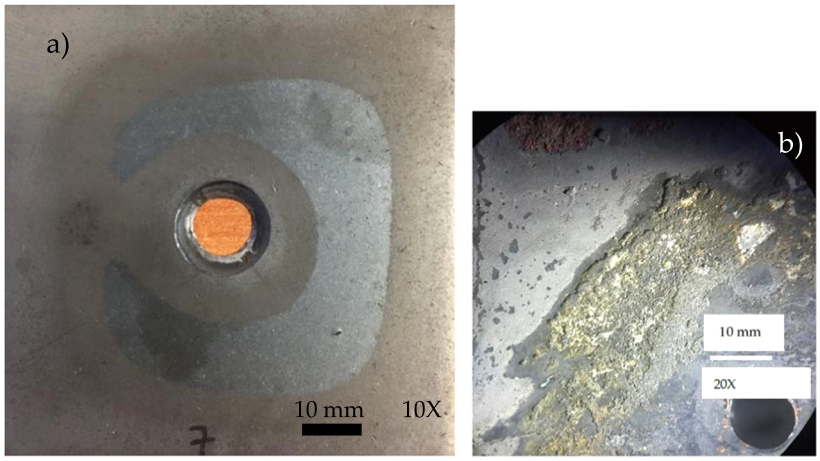

Figure 15. Digital imagines of the tested coupons were exposed to the Geothermal fluid for one month in the Geothermal Unit Los Humeros, Mexico. (a) Ni_3B-TiB_2 coating at 10X and (b) Uncoated SS304 substrate at 20×.

4. Conclusions

Corrosion and wear damage of steam turbines depend on different variables such as steam composition, temperature, and geographic area where is located the geothermal well. High concentrations of sulfides and chlorides are present on geothermal reserves of low temperature, where the frequent mechanism of corrosion are; stress corrosion cracking (SCC) followed by corrosion pitting (P), corrosion flow accelerated (FAC), and erosion (E). The Ni_3B-TiB_2 coating is an excellent example of a metal-ceramic material where the mechanical and chemical stability is attributed to the combination of both phases. The high entropy Ni_3B phase controls the high hardness and high thermal stability of the TiB_2.

In thin films deposited by vaporization, the distance of the interfaces between nanometric crystals with the temperature effect was reduced, producing a more compact coating and maintaining their resistivity with an elastic-plastic behavior to resist adhesive wear. The polarization curves showed that the corrosion rate was low (0.0010 mm*year-1), independent of the exposition time and temperature, while the coating was intact. The nanostructured coating of Ni_3B-TiB_2 deposited by PVD Sputtering reduces their nanoporosity by the temperature effect and exposition time without significantly changing the corrosion rate at 80 °C.

Acknowledgments

This research was developed at the Center of Research and Technological Development in Electrochemistry (CIDETEQ), together with the INNOVACOAT-L research group. We offer unique acknowledge to the Eng. Veronica N. Martínez Escobedo, for their technical support during the coating characterization.

Data availability statement

All data that support the findings of this study are included within the article (and any supplementary files).

Patents

Patent-pending with the Mexican Institute of Industrial Property (IMPI acronym in Spanish) with record number MX/a/2020/002396.

Author contributions

Conceptualization, Investigation, Funding Acquisition, Jorge Morales Hernández; Methodology, Coraquetzali Magdaleno López; Validation, Héctor Herrera Hernández; Writing-Original Draft Preparation, Jorge Morales Hernández; Writing-Review & Editing, José Manuel Juárez García; Project Administration, Data curation, Raúl Herrera Basurto; Investigation, Supervision, Héctor Dorantes Rosales.

Funding

Funding sources: Financial support for this work was provided by CONACYT-SENER through the call Energy Sustainability with the project 259334, from the Mexican government.

Conflicts of interest

The authors declare no conflict of interest. The funders had no role in the design of the study; in the collection, analyses, or interpretation of data; in the writing of the manuscript, and in the decision to publish the results.

ORCID iDs

Jorge Morales Hernández https://orcid.org/0000-0002-8892-128X
José Manuel Juárez García https://orcid.org/0000-0002-2303-5420

References

[1] Li Z, Liu X, Guo K, Wnags H, Cai B, Chang F, Hong C and Dai P 2019 Microstructure and properties of Ti(C,N)-TiB_2-FeCoCrNiAl high-entropy alloys composite cermets *Materials Science & Engineering A* **767** 138427
[2] Xi L, Kaban I, Nowak R, Brizda G, Sobczak N, Stoica M and Eckert J 2016 Investigation of Ni-B alloys for joining of TiB_2 ultra-high-temperature ceramic *J. Mater. Eng. Perform.* **25** 3204
[3] Semenova E, Rokhlin L, Dobatkina T and Kolchugina N 2010 *Boron-Nickel-Titanium. In Refractory Metals Systems* ed G. Effenberg and S. Ilyenkoed 11E2 (Germany: Landolt-Börnstein Group IV Physical Chemistry) 153–62
[4] Wang F C, Zhang C Z H, Luo J, Huang C C and Lee S K 2009 A novel rapid route for *in situ synthesizing TiB-TiB_2 Composites; Compos. Sci. Technol* **69** 2682–7
[5] Derin B, Kurtoglu K, Sahin F C and Yucel O 2017 Thermochemical modeling and experimental studies on the formation of TiB_2 through carbothermic synthesis from TiO_2 and B_2O_3 or B_4C *Ceram. Int.* **43** 10975–82
[6] Nesakumar J I E T, Atchudan R, Karthik N, Gopalakrishnan S M and Rok L Y 2017 Ultrasonic synthesis, characterization and energy applications of Ni-B alloy nanorods *J. Taiwan Int. Chem. E.* **80** 901–7
[7] Huang L, Wang H Y, Li Q, Yin S Q and Jiang Q C 2008 Effect of Ni content on the products of Ni-Ti-B system via self-propagating high-temperature synthesis reaction *J. Alloys Compd.* **457** 286–91
[8] Morales-Hernández J, Escobedo V N M, Hernández H H, García J M J and Palmerin J M 2018 Synthesis of TiB_2-Ni_3B Nanocomposite Powders by Mechanical Alloying. *In Novel Nanomaterials—Synthesis and Applications* ed Z G Kyzas and C A Mitropoulos (London: Intech Open) 37–50
[9] Zhou Y, Li C J, Yang G J, Wang H D and Li G 2010 Effect of self-propagating high- temperature combustion synthesis on the deposition of NiTi coating by cold spraying using mechanical alloying Ni/Ti powder *Intermetallcs* **18** 2154–8
[10] Merk N, Morris D G and Stadelmann P 1987 Crystallization processes in Ni-Ti-B glassy alloys of near-ternary- eutectic-composition *Acta Metall.* **35** 2213–25
[11] Zadorozhnyy V, Kaloshkin S, Kaevitser E and Romankov S 2011 Coating of metals with intermetallics by mechanical alloying *J. Alloys Compd.* **509S** S507–9
[12] Tang W M, Zheng Z X, Wu Y C, Wang J M, LÜ J and Liu J W 2006 Synthesis of TiB_2 nanocrystalline powder by mechanical alloying *Trans. of Nonferrous Met. Soc. China* **16** 613–7
[13] Calka A and Radlinski A P 1990 Formation of TiB_2 by mechanical alloying *J. Less Common Met.* **161** 23–6
[14] Eckert J 1997 Mechanical alloying of highly processable glassy alloys *Mater. Sci. Eng.* **226-228** 364- 373
[15] Joardar J, Pabu S K and Murty B S 2007 Milling criteria for the synthesis of nanocrystalline NiAl by mechanical alloying *J. Alloys Compd.* **429** 204–10

[16] Guozhong C 2004 *Nanostructures and Nanomaterials, Synthesis, Properties and Applications* ed G Cao (London: Imperial College Press) 1–224
[17] Łępicka M and Gradzka-Dahlke M 2019 The initial evaluation of the performance of hard anti-wear coatings on metallic substrates: thickness, mechanical properties, and adhesion measurements—a brief review *Rev. Adv. Mater. Sci.* **58** 50–65
[18] Karolus M and Panek J 2016 Nanostructured Ni-Ti alloys obtained by mechanical synthesis and heat treatment *J. Alloys Compd.* **658** 709–15
[19] Hong Zhao Y-B C 1999 Formation of TiB_2-TiC composites by reactive sintering *Ceram. Int.* **25** 253–8
[20] Loglo F, Innocenti M, Jarek A, Caporali S, Pasquini I and Foresti M L 2010 Niclek sulfur thin films deposited by ECALE: electrochemical, XPS and AFM characterization *Journal of Electrochemical Chemistry* **638** 15–20
[21] Zhang W, Dy S, Li B, Mei T, Miao Y, Chu H and Wang J 2021 Synthesis and characterization of TiN nanoparticle reinforced binary Ni-Co alloy coatings *J. Alloys Compd.* **865** 158722
[22] Sproul W D, Christie D J and Carter D C 2005 Control of reactive sputtering processes *Thin Solid Films* **491** 1–17
[23] XPang X, Zhang L, Yang H, Gao K and Volinsky A 2015 Residual stress and surface energy of sputtered TiN films *J. Mater. Eng. Perform.* **24** 1185–91
[24] Wasa K, Kitabatake M and Adachi H 2004 *Thin Film Materials Technology, Sputtering of Compound Materials* (Norwich, NY, USA: Springer, William Andrew, Inc) 17–111
[25] Martin M P 2010 Handbook of deposition technologies for films and coatings *Science, Applications and Technology* (Norwich, NY, USA: Elsevier. William Andrew, Inc.) 253–96
[26] Bowen R W and Hilal N 2009 Atomic force microscopy in process engineering *In Introduction to AFM for Improved Processes and Products* (Amsterdam: Elsevier) 32–74
[27] González R, Barandika M G, Oña D, Sánchez J M, Villellas A, Valea A and Castro F 1996 New binder phases for the consolidation of TiB_2 hard metals *Mater. Sci. Eng. C* **A216** 185–92
[28] Skordaris G, Bouzakis K D, Kotsanis T, Charalampous P, Bouzakis E, Breidenstein B, Bergmann B and Denkena B 2017 Effect of PVD film´s residual stresses on their mechanical properties, brittleness, adhesion and cutting performance of coated tools *J. Manuf. Sci. Technol.* **18** 145–51
[29] Bobzin K 2017 High-performance coatings for cutting tools *CIRP J. Manuf. Sci. Technol.* **18** 1–9
[30] Fischer-Cripps C A 2004 *Nanoindentation.* (New York: Springer) 147–59
[31] Kumar S M, Chandrasekar P, Chandramohan P and Mohanraj M 2012 Characterization of titanium-titanium boride composites processed by powder metallurgy techniques *Mater. Charact.* **73** 43–51
[32] Wei J, Guo P, Li H, Ke P and Wang A 2022 Insights on high-temperature friction mechanism of multilayer ta-C films 97 *J. Mater. Sci. Technol.* **97** 29–37
[33] Liu J, Chang L, Liu H, Li Y, Yang A and Ruan J 2017 Microstructure, mechanical behavior and biocompatibility of powder metallurgy Nb-Ti-Ta alloys as biomedical material *Mater. Sci. Eng., C* **71** 512–9
[34] Jones A D 1996 *Principle and Prevention of Corrosion* ed Prentice Hall (US: Pearson Education) 143–62
[35] Xu J, Cheng J, Jiang S, Munroe P and Xie Z H 2017 Mechanical and Electrochemical Properties of a sputter-deposited β-$Ta5Si_3$ nanocrystalline coating *J. Alloy Compd.* **Vol. 699**
[36] Jam A, Derakhshandeh R M S, Rajaei H and Pakseresht H A 2017 Evaluation of microstructure and electrochemical behavior of dual-layer NiCrAlY/mullite plasma sprayed coating on high silicon cast iron alloy *Ceram. Int.* **43** 14146–55
[37] Abegunde O, Akinlab E and Oladijo P 2021 Examination of electrochemical corrosion protection of titanium carbide thin film grown by RF magnetron sputtering *Materials today: Proceeding* **44** 994–9
[38] Li K, Yann L, Huang X, Gibson D, Zheng Y, Liu J and Sun L 2017 Surface microstructures and corrosion resistance of Ni-Ti-Nb shape memory thin films *Appl. Surf. Sci.* **414** 63–7
[39] Sun Y, Rong Y, Zhao Y, Zhao Y, Hang R and Yao X 2021 Electrochemical stability, corrosion behavior, and biological properties of Ni-Ti-O nanoporous layer anodically on NiTi alloy *Corros. Sci.* **179** 109104